JOURNAL OF COMPUTATIONAL PHYSICS 121, 142–154 (1995)

Local Simulation of Two-Phase Flows Including Interface Tracking with Mass Transfer

SAMUEL W. J. WELCH

Department of Mechanical Engineering, University of Colorado at Denver, Denver, Colorado

Received February 9, 1994; revised January 19, 1995

This paper presents a moving mesh, two-dimensional finite volume method suitable for tracking interfaces across which there is mass transfer. We consider liquid and vapor phases of single component fluids separated by a phase interface in an evolving flow field. Metastable bulk states are allowed (as are superheated vapor and subcooled liquid bulk states) while the interface is assumed to exist in thermal and chemical equilibrium. Mass transfer occurs at the interface, driven by the local flow conditions. The interface is tracked by nodes representing the liquid and vapor sides at the same spatial location. The interface motion is found from the solution of the coupled interfacial conditions and bulk fluid equations. The bulk fluids are considered as viscous, conducting, and compressible fluids necessitating the use of the continuity, momentum and energy equations in the bulk regions. The control volume continuity, momentum and energy equations are modified in the presence of a phase interface to include surface properties using a simple interface model with surface tension and surface energy. Simple simulations are presented illustrating the method.

I. INTRODUCTION

Two phase flows play an important role in technological processes. An important subclass of two phase flows are flows in which liquid–vapor phase transitions are significant. Heat exchanger equipment and piping in power plants and oil refineries are examples of devices in which phase transitions play an important role. Computational methods for these technologically important processes have traditionally been dominated by the use of averaged equations and their attendant correlations and flow maps. Moe and Bendiksen [19] provide a recent example detailing the use of two-fluid models (a common set of averaged equations). While necessary for the computation of many practical flows, averaged equations do not attempt to resolve the fine scales associated with heat and mass transfer at phase interfaces. Nucleate boiling is an example of a technologically important process in which the small scales associated with the bubble growth and departure are important. There has been extensive experimental work on nucleate boiling but computational methods to accurately address this problem have to date been based on many simplifying approximations. Lee and Nydahl [20] used an assumed bubble shape to simulate the growth and departure of vapor bubbles. Their method neglected any gradients in the vapor phase and required an empirical relationship to complete the geometry. Results of their work have been used in the experimental work of Zeng, Klausner and Mei [21] to aid in the development of a bubble departure model. A similar numerical approach was taken by Patil and Prusa [22] who assumed a hemispherical shape in simulating vapor bubble growth on a heated wall. In order to simulate this type of problem without assuming the bubble shape, it is necessary to include interface tracking capability.

The method presented in this paper is intended for the direct simulation of boiling and condensation phenomenon in two phase flows including the tracking of the phase interface. These flows are characterized by the discontinuity of the normal component of the fluid velocity across a phase interface. In addition, the interface motion is tightly coupled to the surrounding thermal and mechanical fields and gradients which may be discontinuous across the phase interface. Direct simulation including the mass, momentum, and energy transfer across phase interfaces then requires that we resolve these discontinuous fields and gradients as part of the solution algorithm.

We use a semi-implicit finite volume method on a moving mesh. The fluids are viscous, conducting, and compressible with equations of state utilizing pressure and temperature as the independent variables. The state equations are extended smoothly into the saturation region allowing for the existence of metastable states (superheated liquid or subcooled vapor). The interface is tracked with nodes affixed on the liquid and vapor sides at the same spatial location. The interface is embedded within moving control volumes defined on a triangular mesh. The interface motion is found from the physics while the mesh motion in the bulk (single phase) regions is calculated by simple interpolation between the boundaries and the phase interface. While the method presented is two-dimensional, it is extendible to three dimensions provided the analyst is willing to code the extensive geometrical calculations necessary for whatever control volume or grid structure is to be used.

In this paper, we consider flows in which the interface does not distort greatly or change topological features. Extension of our method to flows with large interfacial distortion or change

0021-9991/95 $12.00

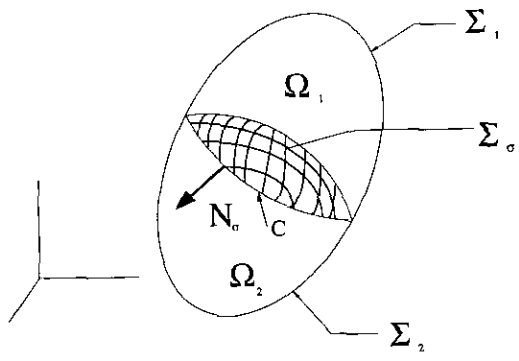

FIG. 1. Region containing two bulk phases separated by a phase interface.

in topology (for example, due to bubbles coalescing) is possible using dynamically restructuring grids such as those found in Fyfe, Oran, and Fritts [13]. We emphasize that such an extension could not compete with Eulerian methods for flows without mass transfer and large interfacial distortion and/or changing interfacial topology. Our method does, however, provide the capability for the direct simulation of local two-phase flows with mass transfer across phase interfaces and the attendant discontinuous fields and gradients. The reader interested in methods suitable for other types of flows will find an excellent review in the paper by Unverdi and Tryggvason [1].

The outline for the remainder of this paper is as follows. We state the governing equations in Section (II), present the spatial discretization of our numerical method in Section (III) and the temporal discretization of our numerical method in Section (IV). Issues related to the mesh motion are discussed in Section (V). We present sample simulations in Section (VI) and close with conclusions in Section (VII).

II. THE BASIC EQUATIONS

We consider a two-phase, non-material, moving region comprised of two bulk regions separated by a phase interface as shown in Fig. 1 (by non-material we mean that the volume and the mass it contains experience different motions). This region occupies the time varying volume $\Omega(t) = \Omega_1(t) \cup \Omega_2(t)$ and is enclosed by the surface $\Sigma(t) = \Sigma_1(t) \cup \Sigma_2(t)$. Bulk phase 1 occupies volume $\Omega_1(t)$ and bulk phase 2 occupies volume $\Omega_2(t)$. The bulk regions $\Omega_1(t)$ and $\Omega_2(t)$ are in contact with the surroundings through the surfaces $\Sigma_1(t)$ and $\Sigma_2(t)$ and are separated by the surface, $\Sigma_\sigma(t)$, which is the phase interface. The phase interface, $\Sigma_\sigma(t)$, intersects $\Sigma(t)$ along the curved line $C(t)$ which divides $\Sigma(t)$ into surfaces $\Sigma_1(t)$ and $\Sigma_2(t)$. $\mathbf{N}_\sigma$ is the outward directed unit normal along $C(t)$ in the tangent plane of $\Sigma_\sigma(t)$. In what follows we write a general set of basic equations for the region $\Omega(t)$, assuming that this region contains two bulk phases along with a phase interface. The basic equations for regions containing a single bulk phase, and therefore no phase interface, are a special case of these general equations. This special case is realized simply by interpreting $\Omega(t)$ as the volume occupied by the bulk single-phase region and $\Sigma(t)$ as the surface enclosing $\Omega(t)$. The interfacial model used in this work requires only a knowledge of the temperature dependence of the surface tension. The surface tension appears in both the momentum and energy equations and a surface energy term appears in the energy equation. Delhaye [3] has shown that failure to include surface properties other than surface tension in the basic equations leads to a violation of the second law for a vapor bubble of decreasing radius. The surface energy is related to the surface tension by a surface constitutive relationship derived from a second law analysis. Further background on this interfacial model may be found in Ishii [8].

The field equations for an arbitrarily moving non-material volume are now expressed in the form used for the finite volume discretization. The continuity equation is expressed as [7]

$$\frac{d}{dt}\int_{\Omega(t)} \rho \, dV + \int_{\Sigma_{(t)}} \rho(\mathbf{v} - \mathbf{v}_s)\cdot \mathbf{n} \, dS = 0, \tag{1}$$

where ρ is the bulk phase density, $\mathbf{v}$ the bulk phase velocity, $\mathbf{v}_s$ and $\mathbf{n}$ are the velocity and outward directed unit normal of the surface $\Sigma(t)$, respectively. The momentum equation is expressed as

$$\begin{aligned}\frac{d}{dt}\int_{\Omega(t)} \rho \mathbf{v} \, dV + \int_{\Sigma_{(t)}} \rho \mathbf{v}(\mathbf{v} - \mathbf{v}_s)\cdot \mathbf{n} \, dS \\ = -\int_{\Sigma_{(t)}} P\cdot \mathbf{n} \, dS + \int_{\Sigma_{(t)}} T^v \cdot \mathbf{n} \, dS + \int_{\Omega(t)} \rho \mathbf{b} \, dV \\ + \int_{C(t)} \gamma \mathbf{N}_\sigma \, dC,\end{aligned} \tag{2}$$

where P is the pressure, T^v the viscous stress tensor, $\mathbf{b}$ is a body force, and γ the surface tension. We note that this equation is our control volume counterpart to the familiar Laplace equation for the pressure jump inside of a gas bubble. The total energy equation is expressed as

$$\begin{aligned}\frac{d}{dt}\int_{\Omega(t)} \rho\left(e + \frac{1}{2}\mathbf{v}\cdot\mathbf{v}\right) dV + \int_{\Sigma_{(t)}} \rho\left(e + \frac{1}{2}\mathbf{v}\cdot\mathbf{v}\right)(\mathbf{v} - \mathbf{v}_s)\cdot\mathbf{n} \, dS \\ + \frac{d}{dt}\int_{\Sigma_{\sigma(t)}} u_\sigma \, dS + \int_{C(t)} u_\sigma (\mathbf{v} - \mathbf{v}_s)\cdot \mathbf{N}_\sigma \, dC \\ = \int_{C(t)} \gamma \mathbf{v}\cdot\mathbf{N}_\sigma \, dC - \int_{\Sigma_{(t)}} P\mathbf{v}\cdot\mathbf{n} \, dS + \int_{\Sigma_{(t)}} \mathbf{v}\cdot T^v \cdot \mathbf{n} \, dS \\ + \int_{\Omega(t)} \rho \mathbf{v}\cdot\mathbf{b} \, dV - \int_{\Sigma_{(t)}} \mathbf{q}\cdot\mathbf{n} \, dS,\end{aligned} \tag{3}$$

where e is the bulk phase internal energy, $\mathbf{q}$ the heat flux vector (assuming Fourier's law), and u_σ is the surface energy. Note that we have tacitly assumed no volumetric energy source. The total energy equation is used instead of the thermal energy

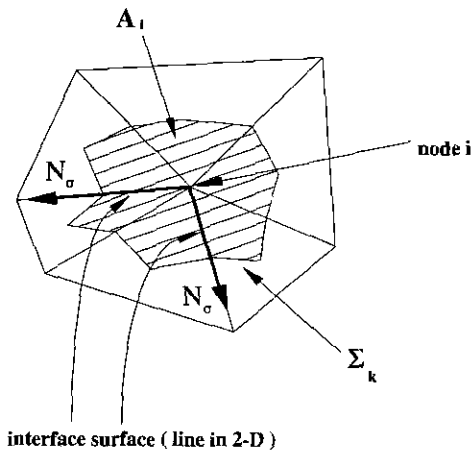

FIG. 2. Discretized two-dimensional region showing triangular mesh and control volume (shaded area).

equation to ensure that the control volume equations will converge consistently to the local interface equations (jump conditions) in the limit as the control volume size vanishes. We note that in the formulation used here, these control volume equations take the place of the classical jump conditions at the interface. We complete the set of basic equations for bulk regions with the bulk state equations,

$$\begin{aligned} e &= e(\vartheta, P) \\ \rho &= \rho(\vartheta, P), \end{aligned} \tag{4}$$

where ϑ is the temperature.

Equations (1) through (4) comprise the set of basic equations for bulk regions. To this set of basic equations we append the relationship between the mesh motion and the control volume area

$$\frac{d}{dt}\int_{\Omega(t)} dV - \int_{\Sigma(t)} \mathbf{v}_s \cdot \mathbf{n}\, dS = 0. \tag{5}$$

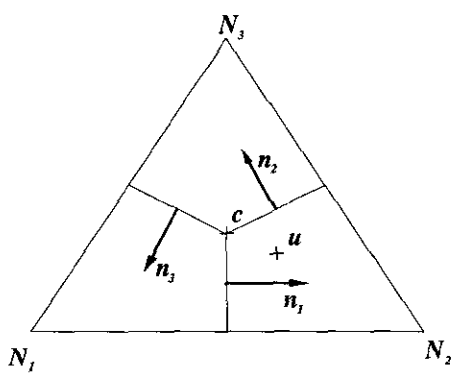

FIG. 3. Triangular element divided into three equal areas.

Equations (1) through (5) comprise the complete set of equations necessary to solve for the flow fields in the bulk regions.

III. ADDITIONAL INTERFACE EQUATIONS

To complete the set of equations for a region containing a phase interface we need the state equations for the interface quantities

$$\begin{aligned} \gamma &= \gamma(\vartheta) \\ u_\sigma &= u_\sigma(\vartheta). \end{aligned} \tag{6}$$

Note that the γ and u_σ are not independent quantities as they are related by the constitutive relationship

$$\gamma = u_\sigma + \vartheta \frac{\partial \gamma}{\partial \vartheta} \tag{7}$$

We also use the interface constitutive equations

$$\begin{aligned} \vartheta_1 &= \vartheta_2 \\ g_1(P_1, \vartheta_1) &= g_2(P_2, \vartheta_2) \\ (\mathbf{v}\cdot\mathbf{N}_\sigma)_1 &= (\mathbf{v}\cdot\mathbf{N}_\sigma)_2, \end{aligned} \tag{8}$$

where the subscripts 1 and 2 refer to the bulk phases, and g is the Gibb's potential for the bulk phases. We note that these interface conditions neglect the irreversibilities associated with heat and mass transfer at the interface. For discussion of these effects and generalizations of Eqs. (8) to the irreversible case

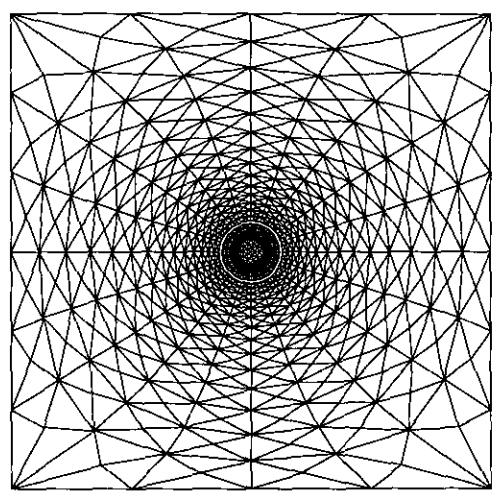

FIG. 4. Computational mesh for first three simulations (vapor nodes slightly compressed to show the initial interface location): 196 vapor nodes; 20 interfacial nodes; 776 total nodes.

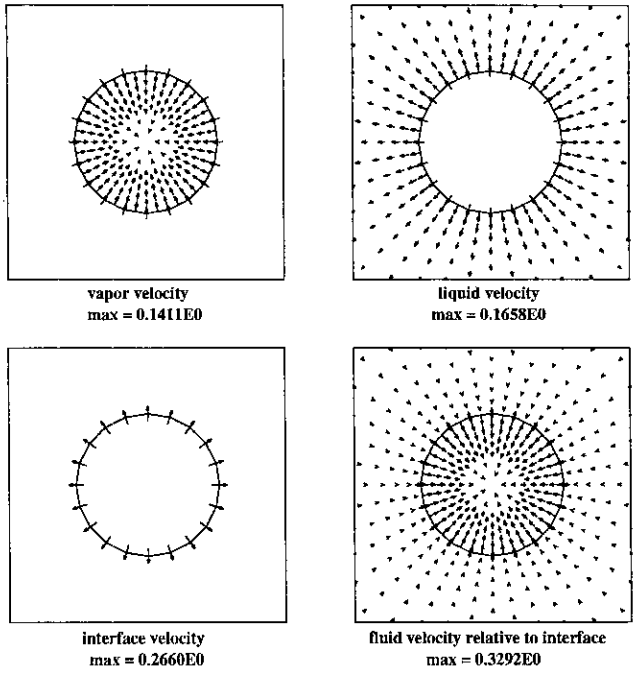

FIG. 5. Fluid velocities at ncyc = 1 for repressurization simulation.

see [8]. The first and second equations of Eqs. (8) are referred to as the thermal equilibrium condition and the chemical equilibrium condition, respectively.

We prescribe the tangential component of the interfacial velocity in such a way as to minimize mesh deformation. The field equations, (1) through (3), may be used to generate the local instantaneous form of the basic equations at the interface (jump conditions) [6]. Inspection of these equations, along with the interface constitutive equations, indicates that the tangential motion of the interface is not determined by physics and may be prescribed arbitrarily.

Mathematically, we consider phase change problems to be moving boundary problems with one phase behaving as an inlet at the interface while the other phase behaves as an outlet. For a fixed boundary problem we would specify three quantities on the inlet side and four on the outlet side [17]. The problem would be closed by the use of a numerical boundary equation on the exit side [18]. For our moving boundary problem we need specify two additional quantities due to the interface motion. We now have four "jump" conditions (Eqs. (1) through (3)), three interfacial equations (Eqs. (8)) and the specification of the tangential interfacial motion. Our formulation then requires the use of two numerical boundary conditions. We have experienced the most success by forcing first or second derivatives of pressure normal to the interface to zero in both phases.

As far as we know, theoretical work on the thermodynamics and fluid mechanics of phase interfaces has still not closed the boundary value formulation of liquid–vapor phase transition problems (thus the need for one extra numerical boundary condition). Dell'Isola and Romano [4, 5] came close to a solution of this problem but still were compelled to postulate an additional constitutive relationship to close their model. We note that the interfacial model used in [4, 5] is much more complicated than that used in our method. The basic physics of interfacial mass transfer is a theoretical area in which there is still work to be done.

IV. SPATIAL DISCRETIZATION OF THE BASIC EQUATIONS

The grid structure used is a typical finite volume grid structure in that the triangular elements are not themselves the control volumes, but rather, contribute to a number of control volumes. Both the scalars and the velocities are defined on the nodes (collocated) as opposed to a staggered arrangement. The advantages of this arrangement are simplicity in forming the control volume equations and the convenience of having the variables defined on the interface. The disadvantage of a collocated grid is the difficulty in controlling $2\Delta\ x$ wavelength modes. The scheme used in this work is analyzed in [2] on a uniform rectangular grid and shown to be stable with a neutrally stable acoustic $2\Delta\ x$ mode at stagnation points.

Shown in Fig. 2 is a typical grid structure of a few triangular elements with the related control volume of node i shown as the shaded area A_i. Also shown is one segment of the control

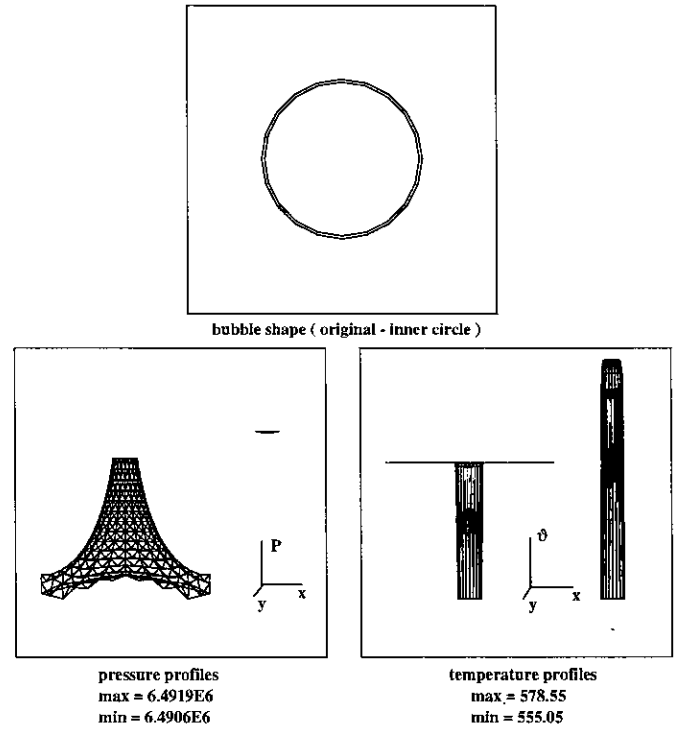

FIG. 6. Bubble shape, pressure, and temperature profiles at ncyc = 1 for repressurization simulation.

surface denoted by Σ_k. The control surface segment Σ_k is defined as a straight line segment from the area centroid of the triangle to the mid-point of the side of the triangle. The control volume in Fig. 2 also contains an embedded phase interface and the tangent plane vector, $\mathbf{N}_\sigma$.

Spatial integrations appearing in the time derivative terms are calculated by lumping the variable at the node as are body force terms in the momentum and energy equations. The surface terms in the equations are built by moving through the grid triangular element by triangular element. This step, typical of the finite volume method, avoids duplication of the surface term calculations for control volumes sharing common boundaries. Consider the triangular element shown in Fig. 3. Here, N_1, N_2, and N_3 are local node numbers on the element while $\mathbf{n}_1$, $\mathbf{n}_2$ and $\mathbf{n}_3$ are normal vectors to the straight line segments opposite of N_1, N_2, and N_3. These straight line segments are the control surfaces Σ_1, Σ_2, and Σ_3 referred to as Σ_k in Fig. 2. The normal vectors have magnitude equal to the length of the straight line segments on which they are defined. Points c and u are the area centroid of the triangle and the upstream coordinate on the triangle calculated as

$$\mathbf{x}_u = \mathbf{x}_c - \frac{\eta}{2}\,\delta t\,\mathbf{v}_c, \tag{9}$$

where $\mathbf{v}_c$ is the velocity of the fluid at the centroid and η is a coefficient whose significance will be discussed later. Unless otherwise stated, the spatial discretizations that follow assume linear profiles on the triangular elements and, if necessary, use area coordinates [12] to form the linear shape functions. In particular, $\mathbf{v}_c$ in Eq. (9) is simply the average of the nodal velocities.

The convective flux terms are evaluated by using the assumed linear profiles on the element for $\mathbf{v}$, $\mathbf{v}_s$, and Ψ. Along each straight line segment Σ_k, we approximate

$$\int_{\Sigma_k} \Psi(\mathbf{v} - \mathbf{v}_s)\cdot\mathbf{n}\,dS \cong \Psi_u \sum_{i=1}^{3} \alpha_k^i\,(\mathbf{v} - \mathbf{v}_s)_{N_i}\cdot\mathbf{n}_k, \tag{10}$$

where Ψ_u is the value of Ψ at the upstream coordinate of the element. We evaluate Ψ at the upstream coordinate to avoid the convective instability typical of a forward time centered space treatment of the convective terms. If we expand the flux terms (written in continuous divergence form) in a Taylor series about the centroidal coordinates, we find

$$\nabla\cdot(\Psi_u\mathbf{v}) \cong \nabla\cdot(\Psi_c\mathbf{v}) - \nabla\cdot(\Lambda\cdot\nabla\Psi_c), \tag{11}$$

where $\Lambda = (\eta/2)\,\delta t\mathbf{v}_c\mathbf{v}_c$ and Ψ_c is the value of Ψ at the centroid. Inspection of Eq. (11) indicates that our treatment of the flux terms is closely related to the tensor viscosity method [9]. We therefore refer to η as the tensor viscosity coefficient. The simulations presented in this paper all use a tensor viscosity coefficient of unity.

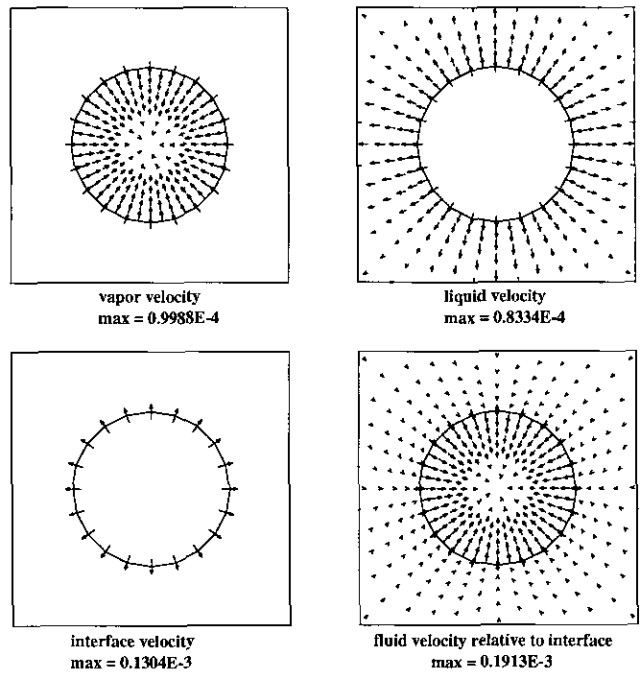

FIG. 7. Fluid velocities at ncyc = 1000 for repressurization simulation.

The coefficient α_k^i in Eq. (10) is calculated using the trapezoidal rule on the velocities along the straight line segment Σ_k of the control surface with outward directed unit normal $\mathbf{n}_k$. The flux terms are then accumulated in the required control volume equations. As will be discussed later, the use of the trapezoidal rule is crucial to satisfying the relationship between the mesh motion and the time rate of change of the control volume area, Eq. (5).

The pressure line integral from momentum is approximated along the straight line segment, Σ_k, as

$$\int_{\Sigma_k} P\mathbf{n}\,dS \cong \sum_{i=1}^{3} \beta_k^i\,P_i\,\mathbf{n}_k, \tag{12}$$

where β_k^i is the coefficient of P_i evaluated using the trapezoidal rule and the assumed linear profile for P. The assumed linear profiles result in constant diffusion and dissipation terms on the triangular elements (but not on the control volume) simplifying a similar surface line integral evaluation. The pressure work term is approximated by expanding the derivative and lumping the coefficient of the resulting gradient and divergence operators. The resulting approximate form is

$$\int_{\Omega(t)} \nabla\cdot(P\mathbf{v})\,dV \cong P_i\int_{\Sigma_{(t)}} \mathbf{v}\cdot\mathbf{n}\,dS + \mathbf{v}_i\cdot\int_{\Sigma_{(t)}} P\mathbf{n}\,dS, \tag{14}$$

where P_i and $\mathbf{v}_i$ refer to the pressure and velocity at the node

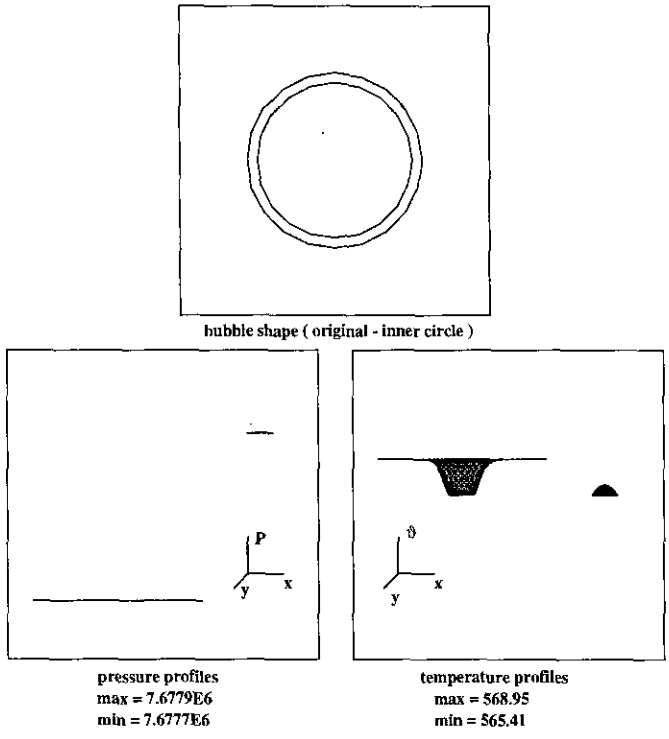

FIG. 8. Bubble shape, pressure, and temperature profiles at ncyc = 1000 for repressurization simulation.

corresponding to the control volume i. The line integrals are then approximated on the element and accumulated in a similar manner as the previous approximations.

The surface tension term in the momentum equation

$$\int_{C(t)} \gamma \mathbf{N}_\sigma \, dC \tag{15}$$

is simple to treat spatially as in two dimensions the term represents a point force acting on the sides of the control volume. The direction of this point force is the direction of $\mathbf{N}_\sigma$ shown in Fig. 2. Consistent with the linear profile in temperature the surface tension is evaluated at the temperature where the interface pierces the control surface. The necessary geometrical calculation for Eq. (15) is the calculation of the unit tangent vector on the interface, $\mathbf{N}_\sigma$. A similar treatment is used for the surface tension work term from the energy equation.

The last term we need to consider spatially is the time derivative of the interfacial surface energy. We use a state equation for γ linear in temperature and Eq. (7) to approximate u_σ as constant. The surface transport theorem [6] then leads to

$$\frac{d}{dt}\int_{\Sigma_\sigma(t)} u_\sigma \, dS = -\int_{\Sigma_\sigma(t)} 2u_\sigma c_n K_m \, dS + \int_{C(t)} u_\sigma \mathbf{v}_s \cdot \mathbf{N}_\sigma \, dC, \tag{16}$$

where c_n is the component of $\mathbf{v}_s$ normal to the interface and K_m is the mean curvature. The second integral on the right-hand side of Eq. (16) is calculated in a manner similar to Eq. (15). The first integral on the right-hand side of Eq. (16) necessitates the calculation of the mean curvature. The interface nodes provide us a convenient coordinate system with which to manipulate the formulae of Weingarten [15] to obtain a (2D) formula for the mean curvature

$$2K_m = -\left(\frac{\partial n_x}{\partial s}\cdot N_{\sigma x} + \frac{\partial n_y}{\partial s}\cdot N_{\sigma y}\right)\Big/ \mathbf{N}_\sigma \cdot \mathbf{N}_\sigma, \tag{17}$$

where n_x and n_y are the cartesian components of the unit normal to the surface, $N_{\sigma x}$ and $N_{\sigma y}$ are the cartesian components of the tangent vector, $\mathbf{N}_\sigma$, and s is the coordinate measured along the interface. The derivatives in Eq. (17) are calculated as centered finite difference formulas using the computational mesh along the interface. This formula is convenient as we have the various normal and tangent vectors stored for other purposes. We now have all of the geometric and kinematic terms necessary to evaluate Eq. (16).

IV. TEMPORAL DISCRETIZATION OF THE BASIC EQUATIONS

Our basic philosophy in the time discretizations that follow is to avoid having to iterate a nonlinear system to advance the solution in time. We therefore linearize our temporal discretizations at the new time level. In order to avoid a Courant limit based on the sound speed we evaluate the pressure in the momentum equations and the velocities in the continuity equation implicitly. We note that these are the spatial terms responsible for acoustic waves. Consistency with the flux terms in the continuity equation requires that we evaluate the velocities in the flux terms of the momentum and energy equations implicitly. As we will be simulating flows in regions where diffusion effects are important we will find it necessary to use computational grids with high mesh resolution in these regions. We therefore treat the diffusion terms implicitly to avoid time step restrictions based on explicit differencing of these terms for higher resolution meshes.

The lumped time derivatives are linearized in time and approximated with forward difference operators. The spatially discretized flux terms, Eq. (10), are linearized in time as

$$\Psi_u^n \sum_{i=1}^{3} \alpha_k^{in} (\mathbf{v} - \mathbf{v}_s)_i^{n+1} \cdot \mathbf{n}_k^{n+1/2}, \tag{18}$$

where $n + \frac{1}{2}$ refers to the average of the $n + 1$ time level and the n time level. The time level on the unit normal will be discussed in a later section. The above terms are linear in the $n + 1$ time level unknowns away from the interface as the mesh motion is known. Flux terms dependent on the unknown mesh motion at the interface are linearized by placing the time

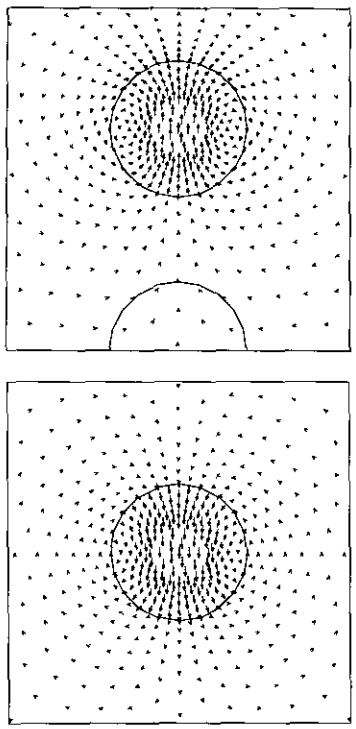

FIG. 9. Velocity field near bubble in thermocapillary simulation at ncyc = 5000. Bottom: mass transfer case, bubble migration velocity = 3.04 mm/s, max fluid velocity = 6.14 mm/s; top: immiscible case—(original bubble position shown at bottom), bubble migration velocity = 0.00 mm/s, max fluid velocity = 0.184 mm/s.

level on the normal vector to time level n. We will use this time linearization for any terms where the new time geometry is unknown due to the control volume either surrounding or being adjacent to the interface.

The viscous dissipation term and body force terms are evaluated explicitly while the pressure work term, Eq. (14), is linearized in time by treating the lumped coefficients explicitly. The surface tension terms in momentum and energy are calculated as implicit terms in temperature. The algebraic interface conditions, Eqs. (8), along with the pressure extrapolations and tangential interfacial motion specification, are treated implicitly and linearized as necessary.

V. MESH MOTION ALGORITHM

The interfacial nodes remain affixed to the interface and their velocity normal to the interface is determined by physics and is found as part of the solution at each time step. The requirement that we move the mesh in the bulk regions comes not from the physics of the problem, but rather, from the desire to limit the amount of distortion in the mesh near the interface due to the interface motion. We seek then an approach that minimizes any additional computational complexity yet satisfies the kinematic Eq. (5). Our approach is to specify the mesh velocity in the bulk regions at time level $n + 1$ in terms of the interfacial mesh velocity at time level n. This allows us to calculate the mesh motion in the bulk regions explicitly while satisfying the kinematic equations. A reasonable scheme is to interpolate the mesh motion in the bulk phases between the boundary nodes (at which the mesh motion is specified) and the interface nodes.

Satisfaction of the kinematic equations is accomplished in the following manner. Consider the area swept out by the motion of one of the straight line segments, Σ_k, during the time interval δt. This area can be shown to be identically [10]

$$\delta A = \frac{\delta t}{4} \mathbf{v}_{s,\text{avg}}^{n+1} (\mathbf{n}^{n+1} + \mathbf{n}^n), \tag{19}$$

where $\mathbf{v}_{s,\text{avg}}^{n+1}$ is the average new time mesh velocity along the segment Σ_k calculated using the linear shape functions on the triangular element. Inspection of Eq. (19) indicates that the kinematic equation, Eq. (5), is satisfied identically in two dimensions if the trapezoidal rule is used for the velocities and the unit normal is the average of the new time and the old time values. This discretization is used for the time derivative of the area and the flux terms in the continuity, momentum, and energy control volume equations. This ensures that the mesh motion is providing no spurious sources to the conservation equations. This is similar to the method used in Demirdzic and Peric [10,

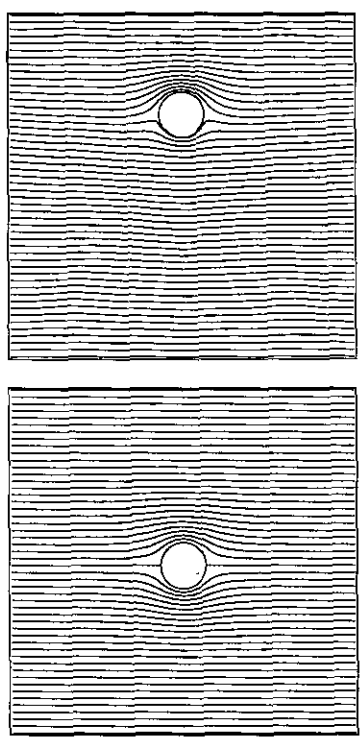

FIG. 10. Temperature contours near bubble in thermocapillary simulation at ncyc = 5000. Center contour value = 568.22 K. Contour increment = 0.2 K. Bottom—mass transfer case; top—immiscible case.

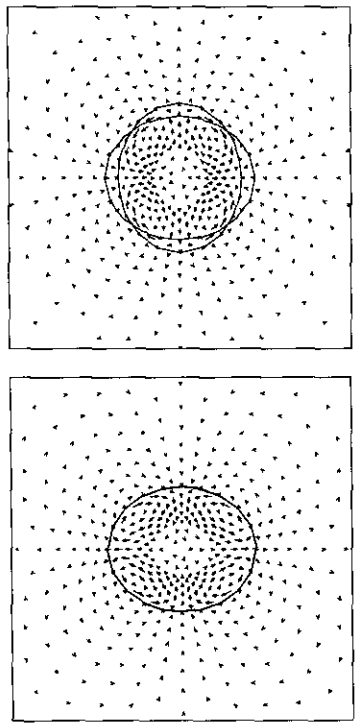

FIG. 11. Velocity field near oscillating bubble (original bubble shape shown with major axis oriented with the horizontal). Top: time = $\tau/2$, max velocity = 4.8 cm/s; bottom: time = τ, max velocity = 4.3 cm/s.

11], who refer to Eq. (5) as the *space conservation law*. We note that the time truncation error in using the old time unit normal is within the time truncation error of the basic scheme (which is first order in time). That this is important will be seen in the following discussion.

The method described above works well for the region of the mesh where there are only bulk phases. If the control volume in question is cut by an interface then the mesh motion algorithm must be modified. We first note that as the interfacial velocity is unknown at time level $n + 1$, the geometry is also unknown. We linearize the discrete equations at the interface by using geometric quantities at time level n.

The latter linearization may also be used in the bulk phases in simulations where it is not clear a priori the best interpolation scheme for the bulk mesh motion. Our approach in the bulk phases is to code formulas stating that the $n + 1$ mesh velocities are simply the average of their $n + 1$ time level neighbors. We call this method the implicit mesh motion method. The disadvantage of the implicit mesh motion method is an increase in storage required for two new equations at each node.

For control volumes containing an interface, Eq. (5) must be applied to regions 1 and 2 separately as the time derivative of these areas is calculated separately. This necessitates the addition of the term

$$[\Psi_1 - \Psi_2] \int_{\Sigma_{\sigma(t)}} \mathbf{v}_s \cdot \mathbf{n}\, dS \tag{20}$$

to the control volume equations, Eq. (1) through Eq. (3). The time level of Ψ_1, Ψ_2, and $\mathbf{n}$ in this equation is n while the time level of $\mathbf{v}_s$ is $n + 1$.

We note that the unknown normal component of the interface velocity appears in the flux terms of the control volume equations at and near the interface. The new mesh positions are determined by a simple explicit Euler step once the mesh (and interface) velocities are known.

VI. SAMPLE SIMULATIONS

We first consider three simulations using the grid shown in Fig. 4. The vapor bubble is 0.02 cm in diameter and the square boundary has sides of length 0.15 cm. There are 196 vapor nodes and 776 total nodes. The length between nodes on the interface is 3.13×10^{-3} cm. The mesh motion in the bulk phases is determined by interpolating linearly in the radial direction between the interface and the boundaries or bubble center. These simulations use a banded matrix direct solver.

We finish with a simulation of a vapor bubble, attached to an adiabatic wall, growing due to mass transfer from the surrounding superheated liquid. We run this simulation on three grids of increasing resolution and compare results.

All simulations use linearized state equations (Eq. (4) and Eq. (6)) formed using properties of liquid and vapor at the reference saturation temperature and pressure of 568.22 K and 8.0 Mpa, respectively. These linearized state equations are obtained simply by estimating the required slopes from the tabular data for water. The same procedure is followed in constructing the surface state equations (Eq. (6)). The tangential interface motion in all simulations is prescribed in such a way as to keep the nodes along the interface as equidistant as possible. The second derivative of pressure is set to zero in the normal direction of the interface by using a simple linear extrapolation along the radial lines emanating from the interface.

Repressurization of a Chamber Due to Vaporization of a Superheated Liquid

We consider first the repressurization of a closed adiabatic chamber of superheated (metastable) liquid in thermal equilibrium with a superheated vapor bubble. The bubble is initially separated from the liquid by a rigid impermeable membrane; hence, the liquid and vapor are not in chemical or mechanical

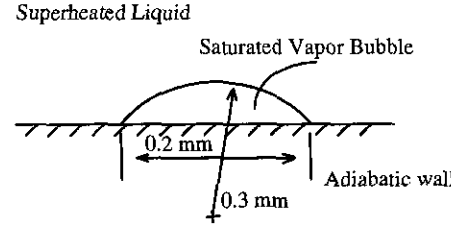

FIG. 12. Initial configuration for simulation of bubble growth on wall.

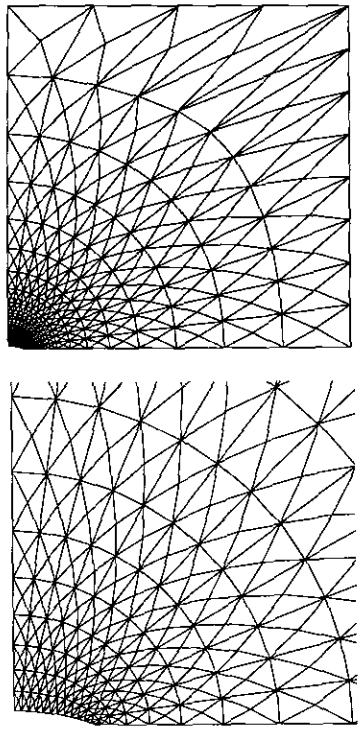

FIG. 13. Medium resolution computational mesh for final simulation (vapor nodes not shown): 264 vapor nodes; 13 interfacial nodes; 652 total nodes.

equilibrium. The liquid and vapor bubble are initially at the superheated state 6.0 MPa, 568.22 K. The membrane is removed and the liquid and vapor make mechanical and chemical contact. We use a time step size of 2.0×10^{-5} s to simulate the transients in this problem as the chamber and vapor bubble are driven to near steady state. The results of this simulation are shown for the first time cycle in Fig. 5 and Fig. 6 and for the thousandth time cycle in Fig. 7 and Fig. 8.

This simulation is driven by the initial inequality of the Gibb's potential at the interface. After the first time step, shown in Figs. 5 and 6, the interface reaches the saturation state shown in the pressure and temperature profiles of Fig. 6 (we note that this saturation state is defined by our linearized state equations and therefore will differ slightly from available tabulated data). The scalar profiles shown in Figs. 6 and 8 have the vapor profiles displaced to the right for clarity with increasing magnitude upwards. Due the vaporization of the liquid, the fluids in the bulk regions are being compressed. The high temperature in the vapor region of Fig. 6 is approximately the adiabatic compression temperature at the shown pressure level. The velocity plots in Fig. 5 indicate that although the liquid is moving radially outward from the bubble, there is still vaporization as the interface is overtaking the liquid.

Inspection of Fig. 6 indicates the existence of a newly formed thermal layer in both the liquid and vapor sides. An interesting phenomenon can be observed in Figs. 6 and 8 concerning this thermal layer. If one considers that, at this temperature, the conductivity of liquid is roughly five times the conductivity of vapor one would expect that the thermal layer on the liquid side would diffuse away faster than the thermal layer on the vapor side. That this is not the case here can be seen from the following simple reasoning. Neglecting surface properties, viscous work done at the interface, and kinetic energy, we may collapse the control volume continuity (Eq. (1)) and total energy (Eq. (3)) equations to the classical jump conditions

$$\dot{m}h_{lg} + \|\mathbf{q}\cdot\mathbf{n}\| = 0 \tag{21}$$

$$\dot{m} = \rho_l(\mathbf{v} - \mathbf{v}_s)_l \cdot \mathbf{n} = \rho_g(\mathbf{v} - \mathbf{v}_s)_g \cdot \mathbf{n}, \tag{22}$$

where h_{lg} is the latent heat of vaporization and $\|\mathbf{q}\cdot\mathbf{n}\|$ is the jump in heat conducted into the interface. Note that the second of these equations reveals explicitly why there is a discontinuity in the normal component of velocity. Inspection of these jump conditions indicates that for the case of a metastable liquid in proximity to an interface, the thermal layer on the liquid side is sucked into the interface while the thermal layer on the superheated vapor side is blown away. This blowing and sucking is visible on the velocity plots (relative to the interface) of Figs. 5 and 7. The temperature profiles in the liquid and vapor regions of Fig. 8 are indicative of this blowing/sucking phenomenon.

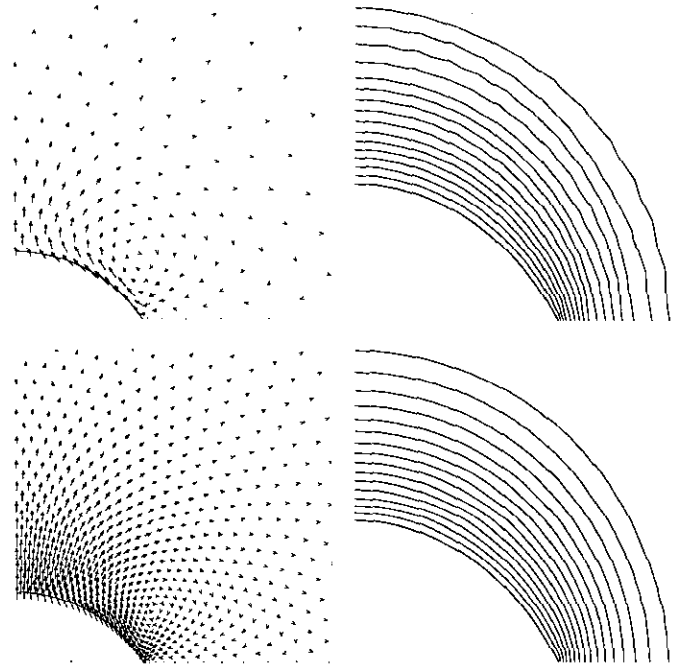

FIG. 14. Liquid velocity field and temperature contours at ncyc = 5000 for final simulation. Inner isotherm is 559.5 K which is the saturation temperature at the bulk liquid pressure. Inner isotherm is the bubble surface. Top left, velocity field for medium grid resolution; top right, temperature contours for medium grid resolution; bottom left, velocity field for fine grid resolution; bottom right, temperature contours for fine grid resolution (temperature contours have 0.5 K increments).

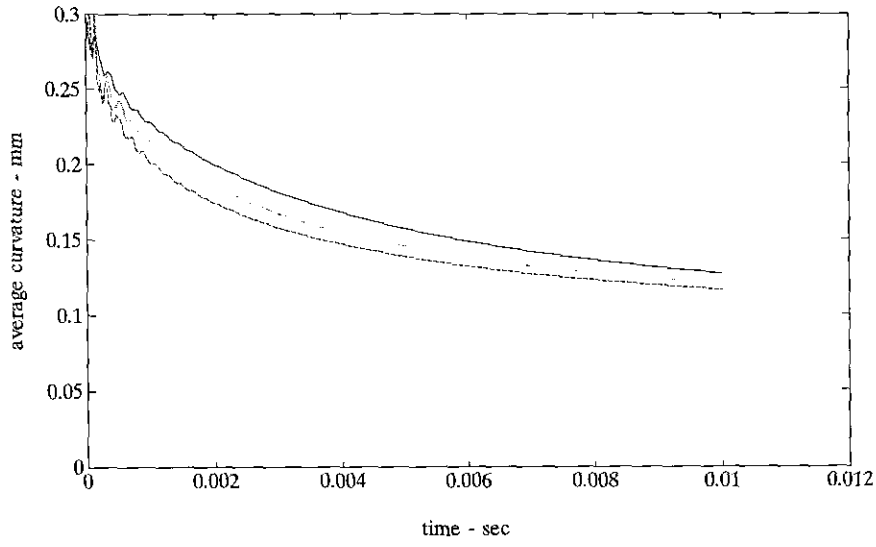

FIG. 15. Average curvatures of bubble surface for three grid resolutions: ——— coarse resolution grid; .... medium resolution grid; – – – – fine resolution grid.

The analytic steady state solution satisfies the conditions of thermal equilibrium, mechanical equilibrium, chemical equilibrium, constant area, constant mass, and constant energy. The numeric values for this analytic steady state solution are found using the same linearized equations of state we use in the code. This final state is $P_g = 8.09695 \times 10^6$ Pa, $P_l = 8.09679 \times 10^6$ Pa, $\vartheta_g = \vartheta_l = 569.066$ K, and the final bubble radius is $a = 1.1441 \times 10^{-4}$ m.

We allow the simulation to execute for 50000 cycles and arrive at the near steady state results $P_g = 8.08438 \times 10^6$ Pa, $P_l = 8.08424 \times 10^6$ Pa, $\vartheta_{\text{interface}} = \vartheta_{\min} = 568.96$ K, $\vartheta_{\max} = 569.03$ K, $a = 1.16 \times 10^{-4}$ m which are in reasonable agreement with the analytic values.

Effect on Thermocapillary Migration of Mass Transfer

We next consider a vapor bubble subjected to a temperature gradient in the surrounding liquid. We compare the resulting flows for an immiscible interface and an interface with mass transfer. The phenomenon of thermocapillary migration occurs when the surface tension is a temperature dependent quantity. For a bubble immersed in a liquid supporting a temperature gradient, thermocapillary migration manifests itself as a motion of the bubble in the direction of increasing temperature [16].

We again use the grid shown in Fig. 4 with the top and bottom walls kept at 5° above and below the reference temperature, respectively. For initial conditions, we have quiescent fluids at a uniform pressure equal to the reference pressure with a linear temperature profile in both fluids between the top and bottom walls. The side walls are adiabatic and the region is closed. These initial conditions are somewhat artificial and we confine our interest to time cycles far removed from the initial transients in which the temperature profile becomes more realistic (nearly uniform in the bubble with the surrounding liquid temperature adjusting itself to the bubble temperature). We use a time step size of 2.0×10^{-5} s in this simulation and Fig. 9 shows the bubble position and velocity profile for the mass transfer case and the immiscible case. The immiscible case is obtained simply by replacing the second of Eqs. (8) with an equation forcing the normal component of one bulk phase velocity and the

FIG. 16. Comparison of bubble size and shape at ncyc = 5000: Fine resolution grid—top shape; Medium resolution grid—middle shape; Coarse resolution grid—bottom shape.

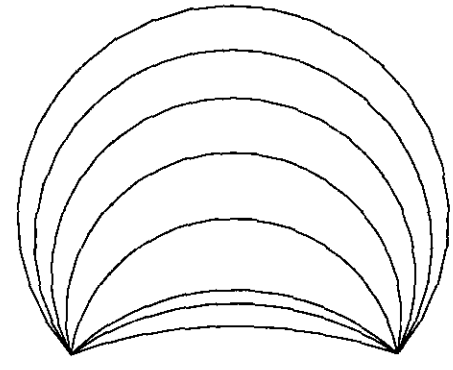

FIG. 17. Bubble shape for final simulation with medium resolution grid time step = 5.0×10^{-6} s. Bubble shapes shown for ncyc = 0, 500, 1000, 5000, 10000, 15000, 20000, and 25000.

TABLE I

Interfacial Velocity at Bubble Mid-Point (mm/s)

Grid \ ncyc	2000	3000	4000	5000
Coarse	2.13	1.93	1.77	1.67
Medium	2.43	2.07	1.87	1.73
Fine	2.49	2.14	1.92	1.77

normal component of the interface velocity to be equal. The control volume continuity equation at the interface will then force the normal component of velocity of the other bulk phase to have approximately the same value. The interface is then material (immiscible).

Viewing Figs. 9 and 10 we make the following observations. The immiscible case, as expected, shows the bubble migrating towards the higher temperature. The bubble with mass transfer has not moved as the effect of the temperature gradient is vaporization of the liquid at the top of the bubble and condensation of the vapor at the bottom of the bubble at the same rate. The resulting temperature field in the bubble is uniform; hence, there is no surface tension gradient driving the thermocapillary migration. As is evident in Fig. 10, the immiscible case still supports a slight temperature profile in the bubble and, hence, a surface tension gradient which drives the thermocapillary migration.

Oscillating Bubble

Next, we consider the oscillations of an elliptically shaped vapor bubble in liquid. Fyfe, Oran, and Fritts [13] obtained an analytic solution for the potential flow case which has become a useful benchmark for testing codes that calculate surface tension effects. We note that this linearized analytic solution is based on small perturbations about the circular shape. For the simulation shown here, the perturbation of shape is finite (10% of the bubble radius), and the full set of basic equations is solved (no approximation based on potential flow is used).

The liquid pressure is set to our reference pressure, the vapor pressure is increased by the surface tension term appearing in the momentum jump (control volume equation) projected in the normal direction. The initial temperature is found by satisfying the equality of the Gibb's potential for the liquid and vapor phases. If there were no perturbation of bubble shape, this set of initial conditions would define an equilibrium configuration. The bubble shape is perturbed to an ellipse with major axis along the horizontal and minor axis along the vertical. The analytic solution mentioned previously predicts a frequency of oscillation

$$\omega^2 = \frac{\gamma(n^3 - n)}{(\rho_l + \rho_g)a^3} \tag{23}$$

which for our parameters indicates a period of oscillation for the lowest mode, $n = 2$, of $\tau = 5.639 \times 10^{-4}$ s. We simulate this with a time step size one-hundredth of the period with Fig. 11 showing simulation results at the fiftieth and hundredth time steps (time steps corresponding to the first half and full periods).

In Fig. 11 we observe that, for this simulation, the analytic solution accurately predicts the period of oscillation (the difference in shape between bubble at the initial condition and at the first period, time = τ, is barely discernible). We also observe that mass transfer in this simulation is insignificant as there is no mechanism by which a significant thermal layer is set up.

TABLE II

Maximum Liquid Velocity (mm/s)

Grid \ ncyc	2000	3000	4000	5000
Coarse	3.59	5.25	8.03	11.9
Medium	3.45	3.74	4.68	6.07
Fine	3.41	2.99	2.87	3.09

Bubble Growth at a Wall

Last, we consider the growth of a vapor bubble attached to a rigid adiabatic wall. Figure 12 shows the initial geometry; the bubble has a curvature of 0.30 mm and the length of the base of the bubble (that part of the bubble attached to the wall) has length 0.20 mm. The vapor is surrounded by superheated (metastable) liquid at 568.22 K, 7.0 MPa liquid. The upper boundary is open to an ambient pressure of 7.0 MPa and the liquid state is initially 568.22 K, 7.0 MPa. The vapor is initialized to the saturation temperature corresponding to 7.0 MPa plus the increase in pressure due to the surface tension. The right side wall is adiabatic and we place a symmetry boundary through the middle of the bubble. Unlike the simulation of bubble growth given earlier, the liquid pressure will not increase as there is an open boundary. The phase interface will then remain near the saturation temperature corresponding to the ambient pressure resulting in a sustained thermal layer. Heat will continually be supplied to the interface, resulting in sustained bubble growth.

This simulation is repeated on three grids of increasing resolution. The coarse resolution grid has seven nodes along the interface with 158 total nodes. The medium resolution grid has 13 nodes along the interface with 652 total nodes and the fine resolution grid has 25 nodes along the interface with 2648 total nodes. Shown in Fig. 13 is the grid with medium resolution (vapor nodes removed for clarity). The element length along the interface for this grid is initially 8.5×10^{-3} mm. The coarse and fine resolution grids have double and half this length, respectively. We use a time step of 2.0×10^{-6} s and simulate

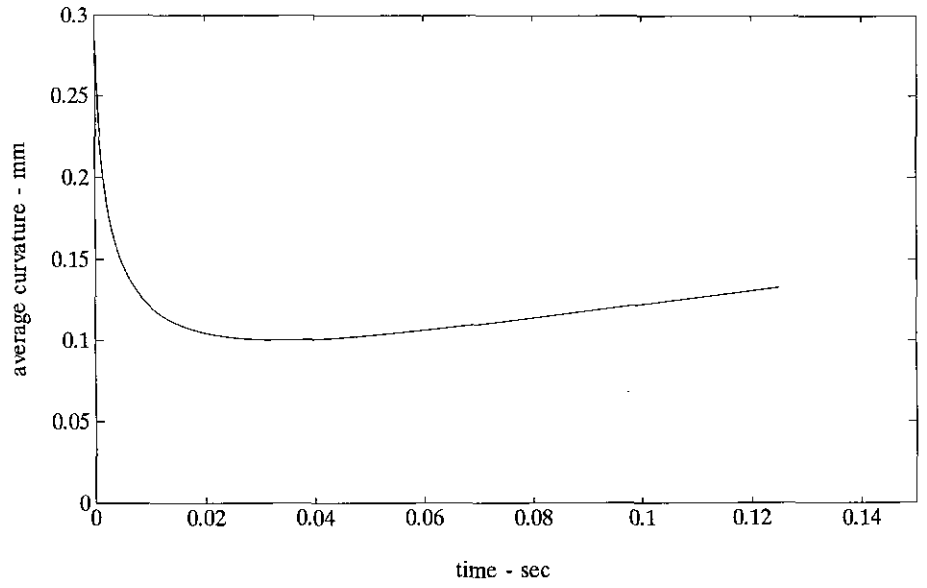

FIG. 18. Average curvature of bubble surface for final simulation with medium resolution grid.

the bubble growth for 5000 cycles. We use the implicit mesh motion algorithm and solve the linear system using an ILU preconditioned transpose-free quasi minimum residual method [23] available in SPARSKIT [24].

Figure 14 shows the liquid velocity fields and temperature contours at the 5000 th cycle for the medium and fine resolution grids. Figure 15 compares the average curvature for the first 5000 cycles of the three cases. The oscillations in curvature apparent in Fig. 15 are similar in nature to those shown in the previous simulation. Figure 16 shows the bubble shape at the 5000 th cycle for the three cases. Table I compares the interfacial velocity of the node originally at the center of the interface for the three grid resolutions. Table II compares the maximum liquid velocity for the three grid resolutions.

Viewing Fig. 14, we note that the temperature field, which drives the mass transfer, is nearly identical for the medium and high resolution cases. We note also that the flow field has similar features. Viewing the numerical data given we see that the convergence of the velocity fields is reasonable during the early stages of the simulation when the bubble sizes and shapes are similar but begins to suffer as the bubble sizes and shapes began to differ. We note that the concept of pointwise convergence does not quite apply here as any fixed point will see a different moving boundary (interface) in the different grid resolution simulations. It is clear that we have not reached grid independent results in this set of simulations.

We close this section by repeating the simulation on the medium resolution grid with a time step of 5.0×10^{-6} s for 25000 cycles. Figure 17 shows the evolution of the bubble size and shape while Fig. 18 shows the average curvature. While the results of the previous simulation indicate that this is not a grid independent result, this simulation does indicate the basic capability to track the interface in nucleate boiling type problems.

VII. CONCLUSIONS

We have presented a method aimed at solving a very specific class of problems. The simulations presented show a basic capability to track interfaces across which there is mass transfer. These simulations also show a basic capability to simulate physics associated with surface tension driven phenomena.

Future efforts will begin with the search for a preconditioner for the iterative method that is optimized for this code. This will allow the use of higher resolution grids when seeking numerically accurate (grid independent) results. Later, the capability to add and remove nodes dynamically would enhance our ability to simulate physics resulting in greater mesh distortions. The long term goal is to use this method to run some "numerical experiments" in axisymmetric nucleate boiling.

ACKNOWLEDGMENTS

This work was supported in part by the Idaho National Engineering Laboratories Long Term Research Initiative in Computational Mechanics. The author also thanks Professor John A. Trapp at the University of Colorado at Denver for his encouragement and support during the difficult periods of this work. The author extends additional thanks to Youcef Saad for the use of the iteration package SPARSKIT2 [24].

REFERENCES

1. S. O. Unverdi and G. Tryggvason, *J. Comput. Phys.* **100,** 25 (1992).
2. S. W. J. Welch, Ph.D. thesis, University of Colorado, 1993.

3. J. M. Delhaye, *Int. J. Multiphase Flow* 1, 395.
4. F. Dell'Isola and A. Romano, *Int. J. Eng. Sci.* **25,**(11–12), 1459 (1987).
5. F. Dell'Isola and A. Romano, *Int. J. Eng. Sci.* **25**(11–12), 1469 (1987).
6. J. C. Slattery, *Interfacial Transport Phenomena.* (Springer-Verlag, New York/Berlin, 1991).
7. J. C. Slattery, *Momentum, Energy and Mass Transfer in Continua*, 2nd ed. (Krieger, Melbourne, FL, 1981).
8. M. Ishii, *Thermo-Fluid Dynamic Theory of Two-Phase Flow* (Eyrolles, Paris, 1975).
9. J. K. Dukowicz and J. D. Ramshaw, *J. Comput. Phys.* **32,** 71 (1979).
10. I. Demirdzic and M. Peric, *Int. J. Numer. Methods Fluids* **8,** 1037 (1988).
11. I. Demirdzic and M. Peric, *Int. J. Numer. Methods Fluids* **10,** 771 (1990).
12. L. Lapidus and G. F. Pinder, *Numerical Solution of Partial Differential Equations in Science and Engineering* (Wiley, New York, 1982).
13. D. E. Fyfe, E. S. Oran, and M. J. Fritts, *J. Comput. Phys.* **76,** 349 (1988).
14. L. E. Scriven, *Chem. Eng. Sci.* **10,** 1 (1959).
15. W. Kosinski, *Field Singularities and Wave Analysis in Continuum Analysis* (Ellis Horwood, Chichester, 1986).
16. N. O. Young, J. S. Goldstein, and M. J. Block, *J. Fluid Mech.* **6,** 350 (1959).
17. B. Gustafsson and A. Sundstrom, *SIAM J. Appl. Math.* **35**(2), Sept. (1978).
18. J. Nordstrom, *J. Comput. Phys.* **85,** 210 (1989).
19. R. Moe and K. H. Bendiksen, *Int. J. Numer. Methods Fluids* **16,** 461 (1993).
20. R. C. Lee and J. E. Nydahl, *J. Heat Transfer* **111** (1989).
21. L. Z. Zeng, J. F. Klausner, and R. Mei, *Int. J. Heat Mass Transfer* **36**(9) (1993).
22. R. K. Patil and J. Prusa, *Experimental/Numerical Heat Transfer in Combustion and Phase Change*, HDT, Vol. 170 (ASME, New York, 1991).
23. R. W. Fruend, *SIAM J. Sci. Stat. Comput.* **14,** 470 (1993).
24. Y. Saad, SPARSKIT2 documentation.